A Three-Dimensional Quasi-Static Model for High Brightness Beam Dynamics Simulation

Ji Qiang, Steve Lidia, and Robert D. Ryne
Lawrence Berkeley National Laboratory,
Berkeley, *CA 94720*

Cecile Limborg-Deprey
Stanford Linear *Accelerator* Center,
Menlo Park, *CA 94309*

In this paper, we present a tinee-dimensional quasi-static model for high brightness beam dynamics simulation in RF/DC photoinjectors, RF linacs and similar devices on parallel computers. In this model. electrostatic space-charge forces within a charged particle beam are calculated self-consistently at each time step by solving the three-dimensional Poisson equation in the beam frame and then transforming back to the laboratory frame. When the beam has a large energy spread. it is divided into a number of energy bins or slices so that the space-charge forces are calculated from the contribution of each bin and summed together. Image charge effects from conducting photocathode are also included efficiently using a shifted Green function method. For a beam with large aspect ratio, e.g. during emission. an integrated Green function method is used to solve the three-dimensional Poisson equation. Using this model, we studied the beam transport in the Linac Coherent Light Sources (LCLS) photoinjector through the first traveling wave linac. The final normalized transverse emittance is below 2 mm $-mrad$ and the uncorrelated energy spread is within a range of a few KeV to about 10 KeV.

I. INTRODUCTION

High brightness, low emittance electron beams from photoinjectors have important applications in next generation light sources and linear colliders. Simplified theoretical models have been used to provide some guidelines for photoinjector design [1–3]. For a systematic machine design and optimization, it still depends heavily on the use of self-consistent computer simulations. A

number of computer models have been used in the past years to simulate beam transport inside photoinjectors [4–12]. As far as we know, a model which can efficiently and accurately handle a three-dimensional beam with large aspect ratio and large energy spread including possible image-charge effects has not previously been available on parallel computers. In this paper, we report on developing a three-dimensional quasi-static particle-in-cell model to simulate the beam transport through the photoinjector using a shifted integrated Green function method for space-charge calculation [13]. Using a shifted integrated Green function, we can accurately and efficiently calculate the three-dimensional space-charge forces of a beam with large aspect ratio and the image charge effects with arbitrary separation using a fast Fourier transform (FFT) method. The large energy spread in the laboratory frame is handled by dividing the beam into multiple energy bins/slices and the space-charge forces are calculated for each slice and are summed together before being interpolated to individual particles. Besides the efficient numerical algorithm for calculation of the 3D space-charge forces, we have also implemented this model on parallel computers using a domain decomposition method. This enables us to run a simulation with both high resolution (e.g. a large number of macroparticles) and fast return time.

II. PHYSICAL MODEL AND COMPUTATIONAL METHODS

The physical model assumed here is a relativistic quasi-static charged particle beam subject to the external acceleration and focusing and the space-charge forces from the beam itself (here, the *quasi-static* means that the static electric field is calculated in the beam frame and both electric and transverse magnetic fields are included in the laboratory frame). Radiation effects of the beam are not included. Comparison studies with and without the radiation effects suggest that the radiation effects should not be significant for the current generation of photoinjectors [14, 15]. The simulation starts by generating a three-dimensional beam bunch behind the photocathode according to the laser pulse length and distribution. This bunch is then moved out of the cathode within the given emission time. During the process of emission, the space-charge forces of particles outside the cathode are included together with external fields from the RF cavity and solenoid magnet. Besides the RF/DC cavity and solenoid magnet beam line elements, the model also includes dipole, quadrupole, sextupole, octupole, and decapole magnets in the beam line element list. The external fields can be supplied in the form of discrete data on a three-dimensional Cartesian coordinate mesh or a cylindrical coordinate mesh. They can also be supplied in the form of Fourier expansion coefficients on the axis when the fields have azimuthal symmetry. These elements can be arranged

with arbitrary longitudinal overlap so that a traveling wave structure (including coupling cells) can be modeled using two overlapped standing wave structures and an input and an output standing wave structures [16].

The particles inside a photoinjector are advanced self-consistently using a particle-in-cell approach. The general equations of motion are:

$$\dot{\mathbf{r}} = \frac{\mathbf{p}}{m\gamma} \tag{1}$$

$$\dot{\mathbf{p}} = q(\mathbf{E} + \frac{\mathbf{p}}{m\gamma} \times \mathbf{B}) \tag{2}$$

where, $\gamma = 1/\sqrt{1-\beta^2}$, $\beta_i = v_i/c$ with $i = x, y, z$, c is the speed of light, m is the rest mass of particle, q is the charge of particle. The electric field, $\mathbf{E}$, and magnetic field, $\mathbf{B}$, include the contributions from external focusing and accelerating fields and space-charge fields of intra-particle Coulomb interactions. For an RF linac, under proper gauge ($\phi = 0$), the external electromagnetic fields in a cylindrically symmetric accelerating structure can be obtained from [17, 18]:

$$\mathbf{E} = -\frac{\partial \mathbf{A}}{\partial t} \tag{3}$$

$$\mathbf{B} = \nabla \times \mathbf{A} \tag{4}$$

where the vector potential $\mathbf{A}$ is given by

$$A_x = \frac{1}{\omega} x \sum_{n=0}^{\infty} \frac{1}{2(n+1)} e_n'(z) r^{2n} sin(\omega t + \theta) \tag{5}$$

$$A_y = \frac{1}{\omega} y \sum_{n=0}^{\infty} \frac{1}{2(n+1)} e_n'(z) r^{2n} sin(\omega t + \theta) \tag{6}$$

$$A_z = -\frac{1}{\omega} \sum_{n=0}^{\infty} e_n'(z) r^{2n} sin(\omega t + \theta) \tag{7}$$

with $r^2 = x^2 + y^2$ and

$$e_{n+1}(z) = -\frac{1}{4(n+1)^2} (e_n''(z) + \frac{\omega^2}{c^2} e_n(z)) \tag{8}$$

where $e_0(z)$ is the electric field on the axis, ω is the RF angular frequency, θ is the initial phase of the RF field with respect to global time zero, and superscript prime denotes the derivative with respect to z. If the RF cavity does not have a cylindrical symmetry, the fully three-dimensional electromagnetic fields are read in from the external supplied data files. The equations of motion are solved using a second-order leap-frog algorithm: the particles are drifted half time step; the particles are collected and deposited onto a three-dimensional grid; the Poisson equation is solved in the beam frame; the electric and magnetic fields are obtained in the laboratory frame through

the Lorentz transformation; the particle momenta are updated using both the space-charge fields and external fields for one time step according to Eq. 2; the particles are drifted another half time step. This procedure is repeated for many time steps until the beam is out of the computational domain.

To calculate the space-charge forces, we solve the three-dimensional Poisson equation. The solution of Poisson's equation can be written as:

$$\phi(x,y,z) \;=\; \frac{1}{4\pi\epsilon_0}\int G(x,x',y,y',z,z')\rho(x',y',z')\;dx'dy'dz' \tag{9}$$

where G is Green's function, ρ is the charge density distribution function. For a high brightness beam inside a photoinjector, the conducting pipe is normally much larger than the size of the beam. In this case, an open boundary condition except near the conducting photocathode can be assumed for the solution of the Green's function in above equation. Here, the Green function is given by:

$$G(x,x',y,y',z,z') \;=\; \frac{1}{\sqrt{(x-x')^2+(y-y')^2+(z-z')^2}} \tag{10}$$

Now consider a simulation of an open system where the computational domain containing the particles has a range of $(0,L_x)$, $(0,L_y)$ and $(0,L_z)$, and where each dimension has been discretized using N_x, N_y and N_z points. From Eq. 9, the electric potentials on the grid can be approximated as

$$\phi(x_i,y_j,z_k) \;=\; \frac{h_x h_y h_z}{4\pi\epsilon_0}\sum_{i'=1}^{N_x}\sum_{j'=1}^{N_y}\sum_{k'=1}^{N_z} G(x_i-x_{i'},y_j-y_{j'},z_k-z_{k'})\rho(x_{i'},y_{j'},z_{k'}) \tag{11}$$

where $x_i=(i-1)h_x$, $y_j=(j-1)h_y$, and $z_k=(k-1)h_z$. As discussed later, a more accurate approximation to Eq. 9 is needed for a beam with large aspect ratio. This is possible by using an integrated Green function method. The computational cost of above convolution by a direct numerical summation can be very expensive and scales as N^6, where N is number of grid points in each dimension. Fortunately, this convolution can be replaced by a cyclic convolution in a double-gridded computational domain:

$$\phi_c(x_i,y_j,z_k) \;=\; \frac{h_x h_y h_z}{4\pi\epsilon_0}\sum_{i'=1}^{2N_x}\sum_{j'=1}^{2N_y}\sum_{k'=1}^{2N_z} G_c(x_i-x_{i'},y_j-y_{j'},z_k-z_{k'})\rho_c(x_{i'},y_{j'},z_{k'}) \tag{12}$$

where $i=1,\cdots,2N_x$, $j=1,\cdots,2N_y$, $k=1,\cdots,2N_z$ and

$$\rho_c(x_i,y_j,z_k) \;=\; \begin{cases} \rho(x_i,y_j,z_k) & :\;\; 1\le i\le N_x;\; 1\le j\le N_y;\; 1\le k\le N_z \\ 0 & :\;\; N_x<i\le 2N_x \;\; or \;\; N_y<j\le 2N_y \;\; or \;\; N_z<k\le 2N_z \end{cases} \tag{13}$$

$$G_c(x_i,y_j,z_k) = \begin{cases} G(x_i,y_j,z_k) & : \ 1\le i\le N_x+1;\ 1\le j\le N_y+1;\ 1\le k\le N_z+1 \\ G(x_{2N_x-i+2},y_j,z_k) & : \ N_x+1<i\le 2N_x;\ 1\le j\le N_y+1;\ 1\le k\le N_z+1 \\ G(x_i,y_{2N_y-j+2},z_k) & : \ 1\le i\le N_x+1;\ N_y+1<j\le 2N_y;\ 1\le k\le N_z+1 \\ G(x_{2N_x-i+2},y_{2N_y-j+2},z_k) & : \ N_x+1<i\le 2N_x;\ N_y+1<j\le 2N_y;\ 1\le k\le N_z+1 \\ G(x_i,y_j,z_{2N_z-k+2}) & : \ 1\le i\le N_x+1;\ 1\le j\le N_y+1; N_z+1<k\le 2N_z \\ G(x_{2N_x-i+2},y_j,z_{2N_z-k+2}) & : \ N_x+1<i\le 2N_x;\ 1\le j\le N_y+1; N_z+1<k\le 2N_z \\ G(x_i,y_{2N_y-j+2},z_{2N_z-k+2}) & : \ 1\le i\le N_x+1;\ N_y+1<j\le 2N_y; N_z+1<k\le 2N_z \\ G(x_{2N_x-i+2},y_{2N_y-j+2},z_{2N_z-k+2}) & : \ N_x+1<i\le 2N_x;\ N_y+1<j\le 2N_y; N_z+1<k\le 2N_z \end{cases} \tag{14}$$

$$\rho_c(x_i,y_j,z_k) = \rho_c(x_i+2(L_x+h_x),y_j+2(L_y+h_y),z_k+2(L_z+h_z)) \tag{15}$$

$$G_c(x_i,y_j,z_k) = G_c(x_i+2(L_x+h_x),y_j+2(L_y+h_y),z_k+2(L_z+h_z))\ . \tag{16}$$

These equations make use of the symmetry of the Green function in Eq. 10. From above definition, one can show that the cyclic convolution will give the same electric potential as the convolution Eq. 11 within the original domain, i.e.

$$\phi(x_i,y_j,z_k) = \phi_c(x_i,y_j,z_k) \qquad for\ \ i=1,N_x;\ j=1,N_y;\ k=1,N_z\ . \tag{17}$$

The potential outside the original domain is incorrect but is irrelevant to the physical domain. Since now both G_c and ρ_c are periodic functions, the convolution for ϕ_c in Eq. 12 can be computed efficiently using an FFT as described by Hockney and Eastwood [19]. The computational cost of this algorithm scales as $N^4\log(N)$ instead of the N^6 in the direct summation.

For a conducting photocathode, the space-charge forces from both the image charge and from the beam itself are included. To find the forces on the beam from the image charge by the standard Green function method, we need to solve the Poisson equation with a computational domain containing both the image charge and the beam. This can be very inefficient since only the fields within the beam are needed and the fields outside of the beam are not used. This inefficiency can be avoided by using a shifted-Green function method [13]. Using the shifted Green function, the center of the field domain (the beam domain) is shifted to the center of the particle domain (the image charge domain). The range of x, y and z covers both the particle domain and the field domain in one computational domain. The shifted Green function is defined as

$$G_s(x,x',y,y',z,z') = \frac{1}{\sqrt{(x_c+x-x')^2+(y_c+y-y')^2+(z_c+z-z')^2}} \tag{18}$$

where x_c, y_c and z_c are the center coordinates of the field domain. The electric potential in the field domain is written as

$$\phi(x+x_c,y+y_c,z+z_c) = \frac{1}{4\pi\epsilon_0}\int G_s(x,x',y,y',z,z')\rho(x',y',z')\ dx'dy'dz'\ . \tag{19}$$

On the doubled computational grid, the shifted Green function is given as:

$$G_{cs}(x_i,y_j,z_k) = \begin{cases} ((x_c+x_i)^2+(y_c+y_j)^2+(z_c+z_k)^2)^{-1/2} & : \ 1\le i\le N_x;\ 1\le j\le N_y;\ 1\le k\ \le N_z \\ ((x_c-x_{2N_x-i+2})^2+(y_c+y_j)^2+(z_c+z_k)^2)^{-1/2} & : \ N_x<i\le 2N_x;\ 1\le j\le N_y;\ 1\le k\ \le N_z \\ ((x_c+x_i)^2+(y_c-y_{2N_y-j+2})^2+(z_c+z_k)^2)^{-1/2} & : \ 1\le i\le N_x;\ N_y<j\le 2N_y;\ 1\le k\ \le N_z \\ ((x_c-x_{2N_x-i+2})^2+(y_c-y_{2N_y-j+2})^2+(z_c+z_k)^2)^{-1/2} & : \ N_x<i\le 2N_x;\ N_y<j\le 2N_y;\ 1\le k\ \le N_z \\ ((x_c+x_i)^2+(y_c+y_j)^2+(z_c-z_{2N_z-k+2})^2)^{-1/2} & : \ 1\le i\le N_x;\ 1\le j\le N_y;\ N_z<k\le 2N_z \\ ((x_c-x_{2N_x-i+2})^2+(y_c+y_j)^2+(z_c-z_{2N_z-k+2})^2)^{-1/2} & : \ N_x<i\le 2N_x;\ 1\le j\le N_y;\ N_z<k\le 2N_z \\ ((x_c+x_i)^2+(y_c-y_{2N_y-j+2})^2+(z_c-z_{2N_z-k+2})^2)^{-1/2} & : \ 1\le i\le N_x;\ N_y<j\le 2N_y;\ N_z<k\le 2N_z \\ ((x_c-x_{2N_x-i+2})^2+(y_c-y_{2N_y-j+2})^2+(z_c-z_{2N_z-k+2})^2)^{-1/2} & : \ N_x<i\le 2N_x;\ N_y<j\le 2N_y;\ N_z<k\le 2N_z\ . \end{cases} \quad (20)$$

The FFT used to calculate the cyclic convolution in Hockney's algorithm can be used to calculate the potential in the shifted field domain using the new shifted Green function. This avoids the requirement that the particle domain and the field domain be contained in one large computational domain. This leads to improved numerical resolution for the charge densities and the resulting electric fields than the conventional method, because the empty space between the charged bunches is not included in the calculation. It is also far more efficient, in terms of computational effort and storage, than the traditional approach of gridding the entire problem domain. To test this algorithm, we have calculated the potential distribution on the axis from the image charge of a round beam as shown in Fig. 1. Here, the 1 nC electron charge has a 3D waterbag distribution with 1 mm rms size and located 5 mm after the cathode. The numerical solution of the electrical potential using the shifted Green function method is given in Fig. 2 together with the analytical solution. It is seen that the numerical solution and the analytical solution agree with each other very well.

The image charge of a beam can have significant effects on the beam quality in photoinjectors. Using the LCLS S-band RF gun [20], we did simulations with and without the image space-charge effects. Here, the initial distribution of electron bunch is a cold $10ps$ long uniform cylinder with $1mm$ radius. The total charge in this bunch is $1nC$. The peak acceleration field is $120MV/m$. Fig. 3 shows the transverse and longitudinal rms sizes of the bunch with and without the image charge effects of the conducting photocathode in the simulation. It is seen that the beam without image charge has a larger initial transverse size than the beam with image charge. The space-charge forces from the image charge of the beam have opposite directions compared with the space-charge forces from the beam itself. This helps to reduce the initial beam blow-up driven by the space-charge forces.

In the above algorithms, both the Green function and the charge density distribution are discretized on the grid. For a beam with aspect ratio close to one, this algorithm works well. However, during the emission of electrons out of the cathode, the beam can have a very large transverse to longitudinal ratio. For example, the typical transverse size is on the order of milimeters while the longitudinal size can be about a few tens to hundred microns. Under this situation, the direct use

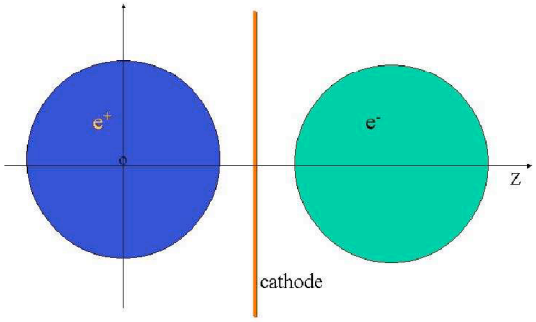

FIG. 1: A schematic plot of an electron bunch in front of the conducting photocahtode together with its image charge.

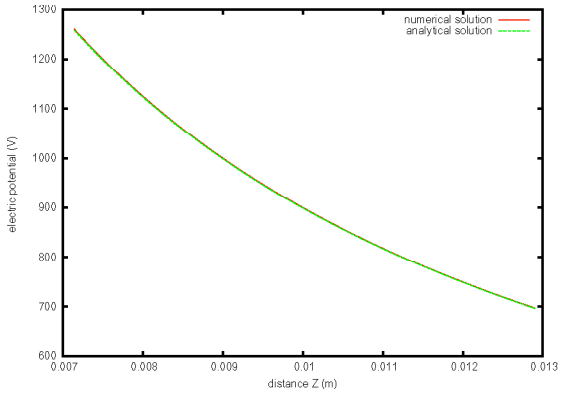

FIG. 2: Image charge electric potential on the axis for a round beam from the shifted Green function solution together with the analytical solution.

of the Green function at each mesh point is not efficient since it requires a large number of mesh points along the transverse direction in order to get sufficient resolution for the Green function along that direction. A two-dimensional integrated Green function method has successfully been used in previous studies of the beam with large aspect ratio [13, 21–23]. Here, we generalize that method to three-dimensional space-charge force calculations. If we assume that the charge density function is uniform within each cell centered at the grid point (x_i, y_j, z_k), we can define an effective Green function as:

$$G_(x_i - x_{i'}, y_j - y_{j'}, z_k - z_{k'}) = \int_{x_{i'}-h_x/2}^{x_{i'}+h_x/2} dx' \int_{y_{j'}-h_y/2}^{y_{j'}+h_y/2} dy' \int_{z_{k'}-h_z/2}^{z_{k'}+h_z/2} dz' G(x_i - x', y_j - y', z_k - z') \quad (21)$$

This integral can be calculated analytically in a closed form:

$$\int\int\int \frac{1}{\sqrt{x^2+y^2+z^2}} dxdydz = yz\ln(x+\sqrt{x^2+y^2+z^2}) + xz\ln(y+\sqrt{x^2+y^2+z^2}) + xy\ln(z+\sqrt{x^2+y^2+z^2})$$

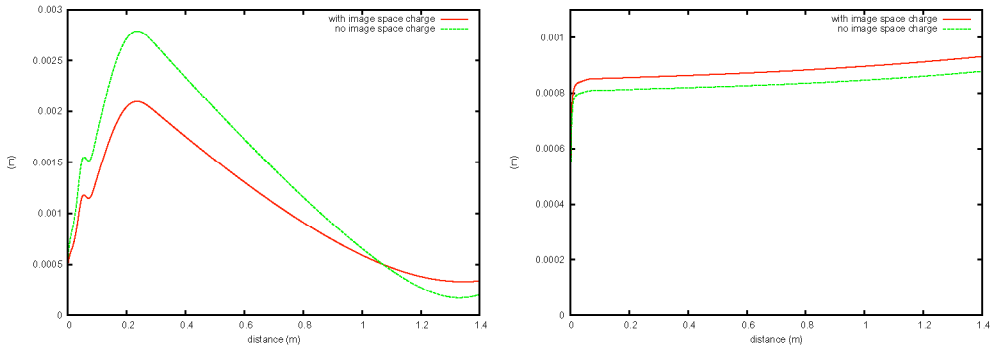

FIG. 3: Transverse (left) and longitudinal (right) rms sizes as a function of distance with and without the image charge effects from photocathode.

$$
\begin{aligned}
&-\frac{1}{4}iz^2\ln\left(\frac{-8ix^2+8(y-iz)-8ix\sqrt{x^2+y^2+z^2}}{x^2(y-iz)z^2}\right)\\
&+\frac{1}{4}iz^2\ln\left(\frac{8ix^2+8(y+iz)+8ix\sqrt{x^2+y^2+z^2}}{x^2(y+iz)z^2}\right)\\
&+\frac{1}{4}ix^2\ln\left(\frac{8(x^2-ixy+z(z+\sqrt{x^2+y^2+z^2}))}{x^2(x-iy)z^2}\right)\\
&-\frac{1}{4}ix^2\ln\left(\frac{8(x^2+ixy+z(z+\sqrt{x^2+y^2+z^2}))}{x^2(x+iy)z^2}\right)\\
&-\frac{1}{4}iy^2\ln\left(\frac{2xy-2i(y^2+z(z+\sqrt{x^2+y^2+z^2}))}{y(x-iy)z^2}\right)\\
&+\frac{1}{4}iy^2\ln\left(\frac{2xy+2i(y^2+z(z+\sqrt{x^2+y^2+z^2}))}{y(x+iy)z^2}\right)
\end{aligned}
\tag{22}
$$

In the above algorithm, we assumed a uniform density distribution within each cell. It is also possible to assume a tri-linear density distribution inside a cell. As a test of this algorithm, we calculated the electric fields along the x-axis and z-axis of a charged beam with uniform density distribution. The numerical results from the integrated Green function together with the solutions from the standard Green function method and the analytical method are given in Figs.4 and 5 for two transverse to longitudinal aspect ratios. Here, $128 \times 128 \times 128$ computational grid points have been used. In Fig. 4, the aspect ratio is one, which corresponds to a uniform spherical ball, all three solutions agree with each other very well. In Fig. 5, the aspect ratio is 30, we can see that the integrated Green function method and the analytical method agree with each other very well. The standard Green function method gives significant discrepancy for the electric field along z-axis, near the edge. For a beam with a Gaussian distribution, the major discrepancy of the electric field occurs around the core, which is given in Fig. 6. These errors in the calculation of electric field for a large aspect ratio beam using the standard Green function method and the integrated Green function method could significantly affect the accuracy of the beam dynamics simulation inside

the RF photoinjector. Fig. 7 shows a comparison of the transverse and longitudinal rms size of an electron beam in the S-band photoinjector using the standard Green function method and the integrated Green function method in the space-charge force calculation using the same number of grid points. The longitudinal rms size from the standard Green function method is significantly larger than that from the integrated Green function method. This is due to an error observed in solving the Poisson equation and calculating the electric field in longitudinal direction using the standard Green function method as shown in Fig. 5 and 6.

In photoinjectors, for a finite length input laser pulse, the electron emitted from the photocathode at head of the beam can have significantly different momentum from the electron at the tail if the acceleration gradient is high. In this case, to calculate the space-charge forces by solving the Poission equation in a single beam frame is not sufficient since there is no single Lorentz transform available in which the spread in longitudinal particle velocities is non-relativistic [24]. If we divide the initial laser pulse into a number of slices, each slice having a very short pulse length, this results in a small velocity spread within each slice. The Poisson equation can be solved in the beam frame of each slice and the electromagnetic fields are Lorentz transformed back to the laboratory frame for each slice. The total space-charge fields at a given location are then added up from the contribution of each slice. Fig. 8 shows the transverse and longitudinal rms sizes of an electron beam with an initial $10ps$ flattop laser pulse and $1nC$ charge in an S-band photoinjector. It is seen that the simulation results converge between two and four slices. The results using only one slice shows about $10-30\%$ different beam sizes at the exit of the gun. This suggests that for such a beam with $10ps$ pulse length, $1nC$ electron and $120MV/m$ peak accelerating field, at least two slices (i.e. energy bins) are needed in order to obtain accurate simulation results.

III. APPLICATIONS

As an application, we have implemented this quasi-static model into a parallel particle-in-cell code, IMPACT-T, to simulate the beam transport through the LCLS photoinjector. The initial laser pulse is assumed to have a 9 ps flat top longitudinal density distribution and a 1 ps Gaussian fall-off near the end of the beam. The transverse density distribution is assumed to be uniform within a round cross section with 1.2 mm radius and 0.72 mm-mrad thermal emittance. The simulation was done using 10^5 macroparticles with $64 \times 64 \times 64$ mesh points and two slices. The photoinjector in this simulation consists of a one-and-half cell 2.856 GHz S-band gun, an 85 cell traveling wave structure, and two solenoid magnets for initial emittance compensation at low

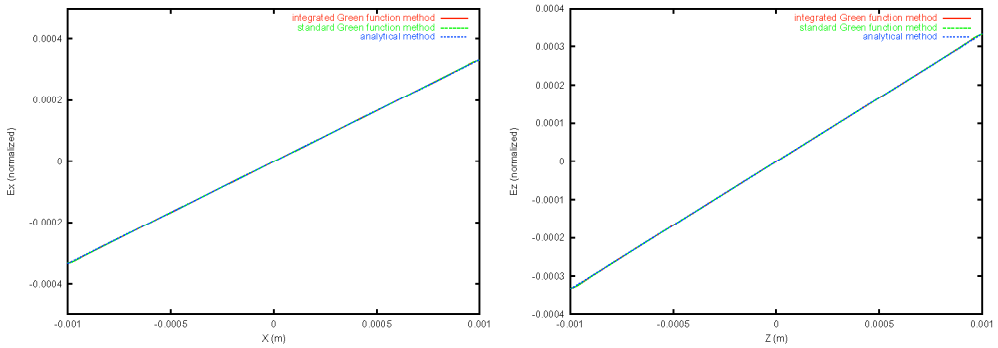

FIG. 4: Electric fields along x-axis (left) and along z-axis (right) of a beam with aspect ratio one from solutions of the integrated Green function method, the standard Green function method, and the analytical method.

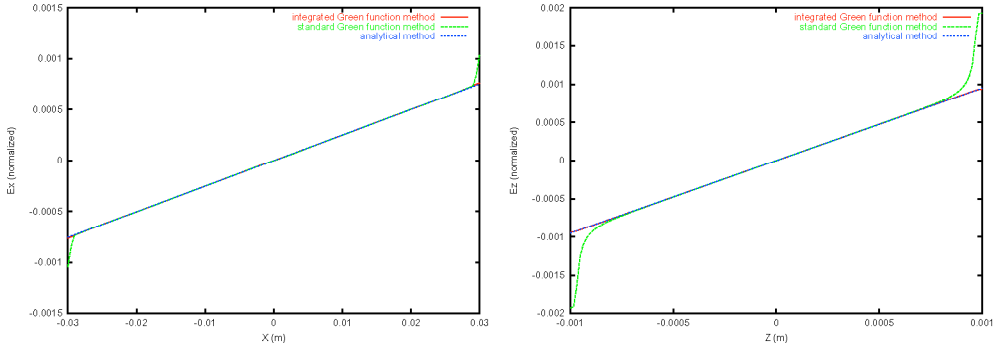

FIG. 5: Electric fields along x-axis (left) and along z-axis (right) of an uniform ellipsoidal beam with aspect ratio 30 from solutions of the integrated Green function method, the standard Green function method, and the analytical method.

energy and transverse focusing [20]. The peak electric field on the cathode is $120MV/m$ and $18MV/m$ inside the linac. The electrons out of the photocathode are accelerated to 62 MeV at the end of the traveling wave structure. To emulate real conditions, we have assumed that the initial laser pulse on the cathode has a $100\mu m$ horizontal offset. This centroid offset is corrected by steering magnets so that at the entrance to traveling wave linac structure, the bunch centroid is set back to zero numerically. The effects of wakefields are not included in this simulation. Fig. 9 shows the normalized rms emittance as a function of distance from the simulation. Here, the rms emittance is caculated using the mechanical momenta of indivdual particles in the laboratory frame. Comparing with the case without initial offset, the transverse emittance is not significantly affected by the initial $100\mu m$ offset. The final projected rms emittance is below 2 mm-mrad. The energy spread of the beam could affect the beam stability and lasing in the LCLS. Fig. 10 shows

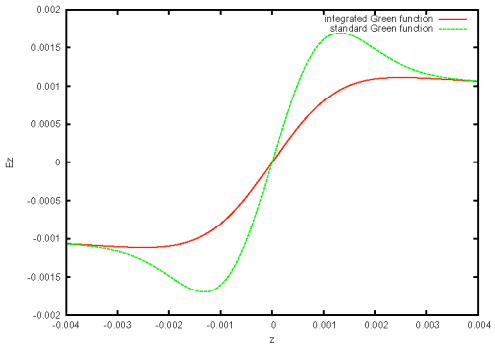

FIG. 6: Electric fields along z-axis of a Gaussian beam with aspect ratio 30 from solutions of the integrated Green function method and the standard Green function method.

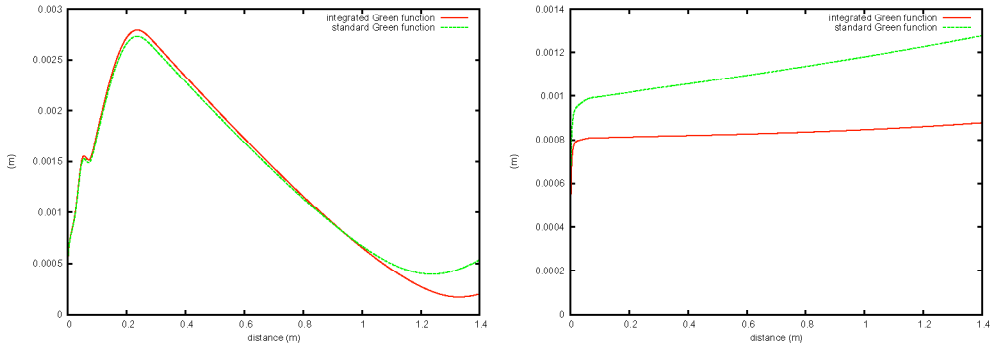

FIG. 7: Transverse (left) and longitudinal (right) rms sizes as a function of distance from the simulation using the standard and integrated Green function method.

the sliced rms energy spread at the entrance to the traveling wave linac with and without the initial offset. It appears that the initial $100\mu m$ offset has no significant effect on the beam energy spread. The uncorrelated slice energy spread increases from the centroid of the beam to the end of the beam. This is caused by the stronger nonlinear fields near the edge of the beam. Fig. 11 shows the uncorrelated sliced rms energy spread at the exit of the first traveling wave linac. The uncorrelated energy spread has decreased in general comparing with that before the linac due to RF acceleration and bunching. The total correlated rms energy spread at the output 62 MeV is about 150 KeV, while the uncorrelated rms energy spread varies from a minimum 3 KeV near the center to 17 KeV at the tail of the beam.

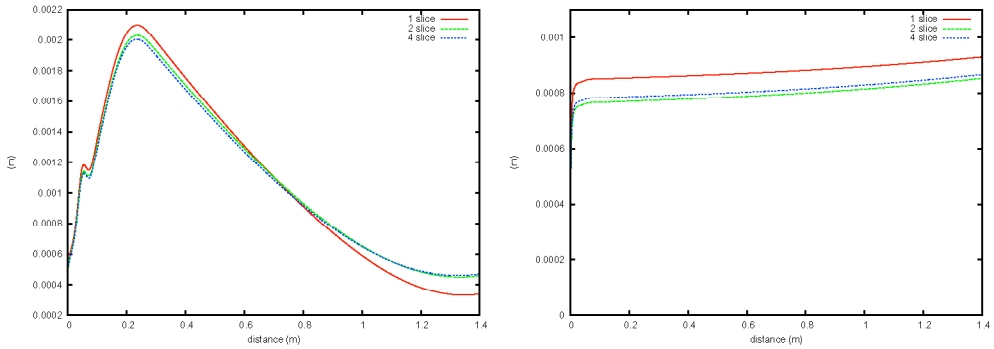

FIG. 8: Transverse (left) and longitudinal (right) rms sizes as a function of distance using one, two and four slices in the simulation.

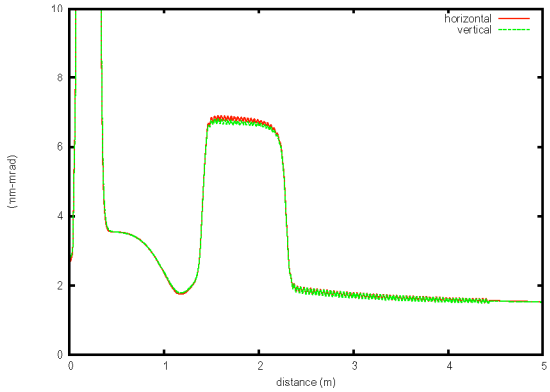

FIG. 9: Transverse normalized rms emittance as a function of distance.

IV. CONCLUSIONS

In this paper, we have presented a three-dimensional quasi-static model for high brightness beam dynamics simulation on parallel computers. The parallel implementation of the model is based on a domain-decomposition method which has been discussed in another publication [25]. It is unique in its use of space-charge solvers based on an integrated Green function to efficiently and accurately treat beams with large aspect ratio, and a shifted Green function to efficiently treat image charge effects of a cathode. This is of major interest to understand the possibility to produce self-generated ellipsoidal photo-electron bunches as proposed by Luiten et al. [26]. In that proposed scenario, ultra-thin sheets of charge would be emitted using a laser pulse as short as 30fs but with a $1mm$ radius. The study of such beams requires a model able to handle very large aspect ratio beams. The model presented in this paper is also unique in its inclusion of energy binning in the space-charge calculation to model beams with large energy spread. Together, all these features

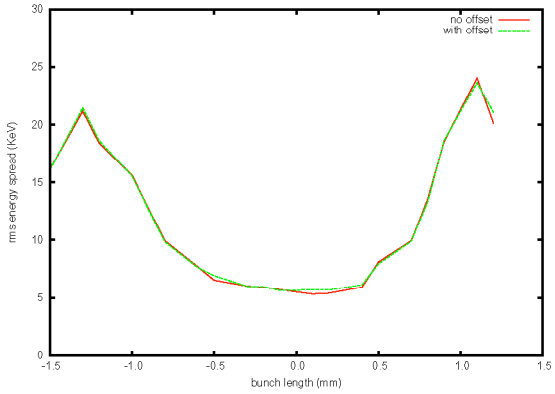

FIG. 10: Uncorrelated rms energy spread at the extrance of the first traveling wave linac with and without initial offset.

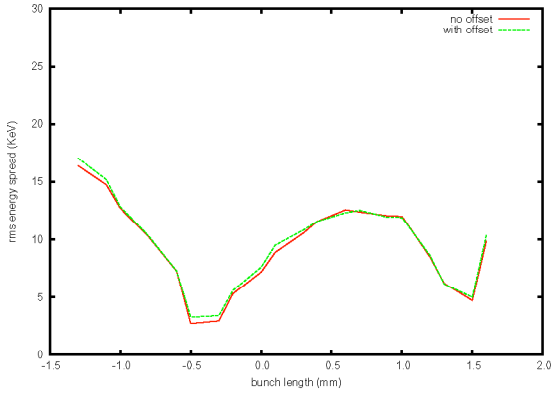

FIG. 11: Uncorrelated rms energy spread after the first traveling wave linac with and without initial offset.

make it a powerful and versatile tool for modeling beams in photoinjectors and other systems. As an application, we have studied a beam transport in the LCLS photoinjector through the first traveling wave linac with an initial $100\mu m$ offset and then steered back to the axis at the entrance of linac. The simulation gives the final normalized transverse emittance below 2 $mm - mrad$ and the uncorrelated energy spread within a range of a few KeV to about 10 KeV. There appears no significant effect from the initial offset of beam at the photocathode.

ACKNOWLEDGMENTS

This research used resources of the National Energy Research Scientific Computing Center, and the resources of the Center for Computational Sciences at Oak Ridge National Laboratory. This work was performed under the auspices of a Scientific Discovery through Advanced Comput-

ing project, "Advanced Computing for 21st Century Accelerator Science and Technology," which is supported by the US DOE/SC Office of High Energy and Nuclear Physics and the Office of Advanced Scientific Computing Research.

REFERENCES

[1] K. J. Kim, Nucl. Instr. and Meth. A 275 (1989) 201.

[2] J. Gao, Nucl. Instr. and Meth. A 297 (1990) 335. (1997) 56.

[3] L. Serafini and J. B. Rosenzweig, Phys. Rev. E 55, (1997) 7565.

[4] L. Young, J. Billen, PARMELA, LANL Codes, laacgl.lanl.gov/laacg/services/parmela.html.

[5] K. Flottmann and P. Piot, Proceedings of EPAC 2002 (Paris), 1798-1800 (2002).

[6] S. B. Van der Geer, M. J. de Loos, Proc. of the 1997 Part. Acc. Conf., Vancouver, Canada, IEEE (1998) p. 2577.

[7] L. Giannessi et al., AIP CP 413 (1997) 301.

[8] J. L. Coacolo et al., Nucl. Instr. and Meth. A 393 (1997) 430.

[9] L. Serafini and C. Pagani, Proc. of IEPAC, Rome, 1998, p. 866.

[10] B. Goplen, et. al., Computer Physics Communications 78 (1995) 54.

[11] Y.Batygin, ISSN 1344-3877, RIKEN-AF-AC-17 (2000), p. 81.

[12] C. Limborg, Y. Batygin, et al., Proceedings of PAC 2003 (Portland), 2003, p. 3548.

[13] J. Qiang, M. A. Furman, R. D. Ryne, J. Comp. Phys. 198 (2004) 278.

[14] L. Serafini, in The Physics of High Brightness Beams, ed. by J. Rosenzweig and L. Serafini, World Scientific (2000), p. 27.

[15] E. Colby, V. Ivanov, Z. Li, C. Limborg, Proc. of the 7th ICAP, Michigan, USA, 15-18 October, 2002, p. 47.

[16] G. A. Loew, R. H. Miller, R. A. Early and K. L. Bane, SLAC-PUB-2295 (1979).

[17] P. L. Morton, Particle Dynamics in Linear Accelerators, Ph. D. Thesis, Midwestern Universityies Reseach Accociation, The Ohio State University, 1963.

[18] S. M. Lidia, Studies of Beam Dynamics in Relativistic Klystron Two-Beam Accelerators, Lawrence Berkeley National Laboratory Report, LBNL-45254, 1999.

[19] R. W. Hockney and J. W. Eastwood, Computer Simulation Using Particles, Adam Hilger: New York, 1988.

[20] C. Limborg-Deprey, S. Gierman, D. Dowell, Proceedings of EPAC 2004, Lucerne, Switzerland, 2004, p. 521.

[21] K. Ohmi, Phys. Rev. E 62 (2000) 7287.

[22] V. Ivanov, private communication, 2003.

[23] R. D. Ryne, in ICFA Beam Dynamics Mini Workshop on Space Charge Simulation, Trinity College, Oxford, 2-4 April 2003.

[24] G. Fubiani and G. Dugan, et al., Proceedings of Advanced Accelerator Concepts, p. 203, 2002.

[25] J. Qiang, R. D. Ryne, S. Habib, V. Decyk, J. Comp. Phys 163 (2000) 434.

[26] O. J. Luiten, S. B. van der Geer, M. J. de Loos, F. B. Kiewiet, and M. J. van der Wiel Phys. Rev. Lett. 93, 094802 (2004).